AIAA JOURNAL
Vol. 40, No. 6, June 2002

Plasma Injection for Hypersonic Blunt-Body Drag Reduction

J. S. Shang*
U.S. Air Force Research Laboratory, Wright–Patterson Air Force Base, Ohio 45433-7913

The summary of combined experimental and computational investigations is presented for the plasma injection from a hypersonic blunt body for drag reduction. The systematic pursuit addresses all speculated mechanisms that can generate favorable magnetoaerodynamic interactions: the counterflow jet shock aerodynamic interaction, the nonequilibrium thermodynamic and chemical phenomenon, and the electromagnetic–aerodynamic interaction. The computational study was carried out by solving both the three-dimensional and the axisymmetric, mass-averaged, Navier–Stokes equations for counterflow jet interaction. The experimental investigation of the plasma injection was conducted in a nominal Mach 6 open jet, blowdown tunnel. The weakly ionized, counterflow jet generated by a plasma torch has a vibrational temperature of 4400 K, an electron temperature around 20,000 K, and electron number density greater than $3 \times 10^{12}/\text{cm}^3$. It is found that the drag reduction is mostly derived from the viscous–inviscid interaction of the counterflow jet and thermal energy deposition. The nonequilibrium and the electromagnetic effect by an applied magnetic field are negligible.

Nomenclature

B = magnetic flux density
D = total drag
E = electrical field strength
J = electric current density
p = pressure
R = radius of hemispheric nose
S = interaction parameter, $\sigma B^2 Rz/\rho u$
T = temperature
U = conservative variables
ρ = air density
σ = electrical conductivity

I. Introduction

ELECTROMAGNETIC force shows promise in being the long-sought-after mechanism for improving the aerodynamic performance of aerospace vehicles.[1–3] The most effective performance improvement using electromagnetism has been demonstrated via the modified Rankine–Hugoniot condition across a shock. In that, the Joule heating and the work done by the Lorentz force on gas particles have been shown to be additional entropy alteration mechanisms.[4–6] However, the possibility of reducing entropy jump and, thus, the wave drag, depends on the strength and polarity of an applied magnetic field, the electrical conductivity of the fluid medium, and the interaction of the aerodynamic and electromagnetic force. For flow control over the entire range of flight, the nonintrusive electromagnetic force is the most cost effective when applied at the onset of any convective instability, where the required electromagnetic force is minuscule. However, there is a prerequisite for this force in aerodynamic applications. The flow medium must be electrically conducting. In a hypersonic stream, the air frequently attains a weakly ionized state in the shock layer, but not upstream of the shock. Hence, the desired interaction may not be achievable by applying an electromagnetic field. Nevertheless, the relative importance of aerodynamic and electromagnetic force is measured by the magnetic interaction parameter, $S = \sigma B^2 L/\rho u$ (Ref. 1). The applied magnetic field strength B and the electrical conductivity of the weakly ionized air σ dominate the interaction.

The first significant magnetoaerodynamic interacting phenomenon was demonstrated by the pioneering work of Ziemer.[7] He has shown the shock standoff distance over a blunt body increased drastically, by a factor of 7.5 for an interaction parameter of 69. In his experimental effort, the aerodynamic force was not measured. However, earlier theoretical studies by Bush[8] and Meyer[9] have shown that the interaction of the electrically conducting fluid with an applied magnetic field can produce appreciable changes of surface heat transfer in plasma streams.

A group of experiments using plasma injection from the stagnation region of a blunt body reported an astonishing amount of drag reduction.[10–12] Although the applied magnetic field was conspicuously absent from these experiments, the counterflow jet interaction, electromagnetic forces, and nonequilibrium thermodynamics were postulated as possible key contributing mechanisms for aerodynamic drag reduction via plasma injection. In more recent research efforts by Shang et al.,[13,14] a major portion of the observed wave drag reduction was shown to be the consequence of the counterflow jet and bow shock interaction. The drag reduction of the counterflow jet and shock interaction is realized by altering a single bow shock to a multiple-shock structure. The shock bifurcation phenomenon was also discovered by the experimental study of the jet spike.[13] At the lower injection mass flow rate, the modified shock envelope is generally conical, and the flowfield is in a self-sustained oscillatory motion.[13–16] At higher injection rates, the displaced shock actually retracts back from the conical to a blunt formation and returns to steady state.[13,14]

Because plasma injection involved weakly ionized gas, the plasma is generally not in a chemical and thermodynamic equilibrium state. It is natural to speculate that the nonequilibrium thermodynamics may contribute to the drag reduction mechanism. Research in hypersonic flow indicates that the dissociated or ionized gas in the shock layer of a blunt body has significant influence on heat transfer, through the recombination of radicals, to deposit the heat of formation at the body surface, but not the wave drag.[17,18] Again, for conventional hypersonic flows over a blunt body, the dissociated or ionized gas is generated by the bow shock compression. Therefore, the plasma only exists downstream of the bow shock. If a microwave or electron beam energy deposition process is used, the ionized gas will then be present upstream of the bow shock. Then the possibility of nonequilibrium thermodynamic phenomenon for drag reduction may be derived from the modified Rankine–Hugoniot jump condition. Recently, Josyula used master equations to investigate the kinetic depletion rate between and within vibrational internal degrees of freedom in nonequilibrium hypersonic blunt-body flows.[18] In his computations, the nonequilibrium flow is imposed as the upstream

Received 18 July 2001; revision received 16 December 2001; accepted for publication 16 December 2001.

*Leader and Senior Scientist, Center of Excellence for Computing Simulation; currently Research Professor, Department of Mechanical and Materials Engineering, Wright State University, 3640 Colonel Glenn Highway, Dayton, OH 45435-0001. Fellow AIAA.

boundary condition. For a given range of freestream translational and vibrational temperatures, computational results show that the nonequilibrium thermodynamic condition has an insignificant effect on the Rankine–Hugoniot jump condition across shock waves.

The blunt body in hypersonic, weakly ionized air with an applied electromagnetic field constitutes the true magnetoaerodynamic phenomenon.[1,7] In the earlier and the present experimental arrangement, the applied magnetic field is generated either by a coaxial pulsed magnet coil or permanent magnets in the blunt body.[5,6,14] The polarity of the applied magnetic field, thus, is aligned closest with the axis of the blunt body instead of a transverse field. Therefore, the drag of the blunt body shall remain nearly unaltered for a weak applied or induced electromagnetic field. The present effort attempts to verify this point and to quantify, if possible, the variation of the drag on the blunt body in conjunction with the magnetic interaction parameter S.

The present investigation concentrates on the understanding of the counterflow plasma injection in hypersonic stream. A side-by-side experimental and computational approach will focus on plasma injection from a hemispherical cylinder at a freestream Mach number of 5.8. Experimental measurements include schlieren photographs, axial aerodynamic force component measurements, and the spectral data of aerodynamic load sensors under tested conditions. The numerical simulations are obtained by solving the three-dimensional and axisymmetric, compressible Navier–Stokes equations based on the unstructured grid technique. The calculations are focused on the stagnation region, and only turbulent solutions by a one-equation closure model are generated. The detailed flow structure within the displaced shock layer will be investigated by comparing the numerical results with experimental observations. The transport properties of the plasma field will also be described in detail.

II. Experimental Facility

The counterflow plasma jet is tested in a blowdown, open-jet, high-Reynolds-number wind tunnel. This wind tunnel was designed to simulate flows at a nominal Mach number of 6.0, at the stagnation temperature of 610 K (1100°R) and a range of stagnation pressures from 3.44×10^2 to 1.40×10^4 kPa (50 to 2000 psi). The mass flow rate of the experiment spans a range from 0.77 to 4.63 kg/s. The blunt-body model is a hemispherical cylinder that has a nose radius and a total length of 38.1 and 203.2 mm (1.5 and 8.0 in.), respectively.

The model for plasma injection was fitted with a conical nozzle to accommodate the plasma torch. To be compatible with the energy input to the air supply of the torch, three nozzles with different throat diameters were used for the experiment: $d = 0.76$, 1.56, and 2.44 mm. However, the plasma injection data were collected only from the nozzle with the smallest diameter. This nozzle has a length-to-diameter ratio of 6.42 and an exit Mach number of 3.28. At the injection stagnation pressure of 482.6 kPa (70 psi) and temperature of 294 K (529 R), respectively, the calculated mass flow rate is 0.52 g/s (0.0011 lbm/s). For the plasma torch experiment, the stagnation pressure input to the torch has an operational range from 482.6 to 965.2 kPa (70 to 140 psia). The range of mass flow rate is below the critical point of the counterflow jet bifurcation for this nozzle. Therefore, the plasma torch experiments were tested exclusively in the unsteady flow regime.[13,14]

In the present investigation, the tunnel is operated at the lowest freestream density of 0.0118 kg/m^3 (0.00074 lbm/ft^3), which still yields a mass flow rate of 0.77 kg/s and the freestream pressure of 2 torr. To circumvent the condensation of the air in the test section, the stagnation temperature is maintained at a constant value of 610 K and the static temperature of 79 K (142.2°R) for all cases studied. Under this tested condition, the Reynolds number has a value of 4.52×10^4/m (1.38×10^6/ft). Additional information of the testing environment can be found in Refs. 13 and 14.

For the plasma injection, the counterflow ionized air is generated by a plasma torch embedded within the model and issues from the stagnation point. The aerodynamic force is collected by a set of three piezoelectric force sensors or load cells. Figure 1 shows a composite picture of the model in the testing condition. The top half of Fig. 1 consists of the video image of the plasma torch in

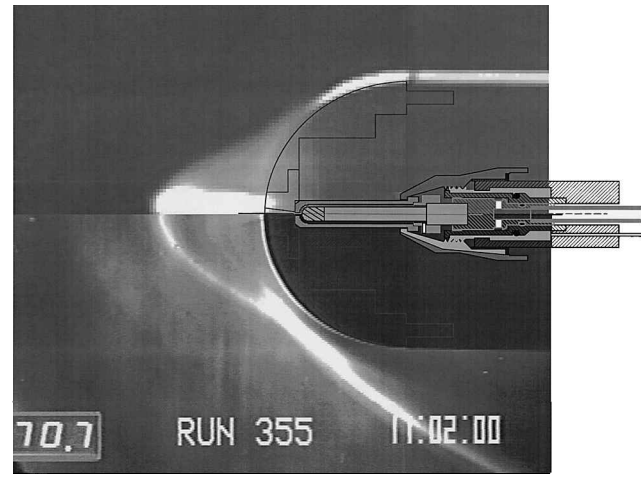

Fig. 1 Force measuring model.

operation, the lower half of the composite is the schlieren of the same test. Overlaid on top of these two images is the sketch of the plasma torch. The model support and installation of the load cells are straightforward; therefore, they are not included in Fig. 1. In essence, the test model is isolated from the tunnel support strut by these load cells to receive the total axial aerodynamic force exerted on the model. To completely describe the plasma injection phenomenon, the thermodynamic properties of the plasma are collected by an emission spectrometer for gas temperature, and a double langmuir probe for electron density and electron temperature.

A plasma cutting torch from Thermadyne supplies the ionized air for the counterflow jet. This torch consists of two basic units: the PAK Master 50XL power supply and the PCH/M-28 torch. The maximum rated output from this plasma torch is 35 A, with an ac input single-phase voltage of 208. However, in the present application, the unit is strictly operating in the starting mode. Therefore, the power output is far below the rated value. The arc starting circuit has a high-frequency generator that produces an ac voltage from 5000 to 10,000 V at a frequency of approximately of 2 MHz. The pilot arc within the torch head is initiated in the gap between the cathode and the positively charged tip. The pilot arc ionizes the compressed air passing through the torch head and exits through a small orifice in the torch tip with a swirling velocity component. The plasma is further expanded by a conical nozzle built in the model. The plasma jet exits the nozzle at a Mach number of 3.28 if a sonic condition prevails at its throat and the nozzle flows full.

The aerodynamic force was measured by load cells and later verified by a strain gauge. For most experiments, three load cells were used to record the total aerodynamic force along the body axis. These load cells, or quartz-force rings (ICP Model 201B03) have a maximum compression range of 11.1 kN and a sensitivity of 44.4 N. The force data recorded by these cells was a prestressed load of 2.2 kN necessary to operate in the linear measuring range. To minimize the electrical signal interference for the magnetoaerodynamic experiment, the force measurement was validated by a strain gauge through a pivot hinge at the base of the model support. Data collected by both measuring devices showed close agreement. By this arrangement, the total axial force exerted on the entire model, including the wave drag, skin-friction drag, base drag, and the reverse thrust of the counterflow jet is obtained.

III. Numerical Analysis

An experimental, computational side-by-side investigation is essential for studying the complex self-sustained fluid motion highlighted by a jet spike shock bifurcation. The detailed dynamic event of the counterflow jet and its associated multiple shock wave structure can only be obtained by solving the time-dependent, three-dimensional, and axisymmetrical Navier–Stokes equations. The system of governing equations is solved by an implicit, unstructured Euler/Navier–Stokes solver for perfect gas called Cobalt.[19] The numerical algorithm is based on the Godunov's Riemann formulation and implicit time stepping to yield second-order spatial

and temporal accuracy.[20] The numerical procedure is developed for a cell-centered, finite volume approach and is able to accommodate a single-grid system that may consist of a variety of cell types, tetrahedron and hexahedron, in three-dimensional space. The neighbor-cell connectivity of an unstructured gird formulation also enhances an exceptionally scalable, parallel computing performance when this numerical procedure is ported to multicomputers using a message passing interface (MPI) library.[21]

The governing equations are discretized by the fully implicit numerical scheme as

$$[3(\boldsymbol{U}^{n+1} - \boldsymbol{U}^{n}) - (\boldsymbol{U}^{n} - \boldsymbol{U}^{n-1})]/2\Delta t + \nabla \cdot \boldsymbol{F} = 0 \qquad (1)$$

where U are the conservative independent variables $U(\rho, \rho u, \rho v, p)$ and $\boldsymbol{F}$ are the flux vectors of the Navier–Stokes equations. The reconstruction of the flux vectors at the centroid of the cell faces is by a least-square solution to the following approximation:

$$\boldsymbol{U}_{i\pm\frac{1}{2}} = \boldsymbol{U}_i \pm \bar{r} \cdot \nabla \boldsymbol{U}_i \qquad (2)$$

where $\boldsymbol{U}_{i\pm 1/2}$ are the reconstructed left and right side of the variables at the cell interface and $\nabla \boldsymbol{U}_i$ is the gradient vector for the cell i.

In the present application, the no-slip velocity components and adiabatic temperature conditions are imposed on the blunt-body surface. For the plasma torch, the sonic throat is prescribed as the entrance boundary for the conical nozzles in the computational domain. The unperturbed freestream condition is specified at the upstream boundary and the no-reflection condition downstream for the far field. Turbulent closure is achieved by the Spalart–Allmaras one-equation model.[22]

The numerical accuracy is assessed by generating four consecutive solutions on increasingly refined grids. For the shock-dominant problem, the error criterion for evaluation is the shock definition and the standoff distance. At a freestream Mach number of 5.8 and a Reynolds number based on nose diameter of 3.45792×10^5 the axisymmetrical flowfield around the hemispherical cylinder is calculated on four different grid systems that consist of 12,699; 23,724; 37,395; and 68,248 cells. For three-dimensional calculations, three grid systems of 185,484; 256,824; and 303,804 cells are used. Similar numerical accuracy assessments also performed for all other nozzles used.

In Fig. 2, the pressure distributions in the supercritical state of the $d = 2.44$ mm nozzle are presented. The numerical results depict the change along the axis of symmetry from the undisturbed freestream toward the blunt body. These pressure distributions reveal the rapid compression and expansion process at the bow shock and the forward motion terminating Mach disk. The pressure distribution also shows the final and continuous expansion from the counterflow jet exit into the shock layer. The numerical results are essentially grid independent after the third grid refinement. The calculated and measured standoff distances without injection compare very well with the correlated data by Ambrosio and Wortman.[23] The normalized values by the nose radius are $\Delta/R = 0.155$ and 0.157, respectively.[13]

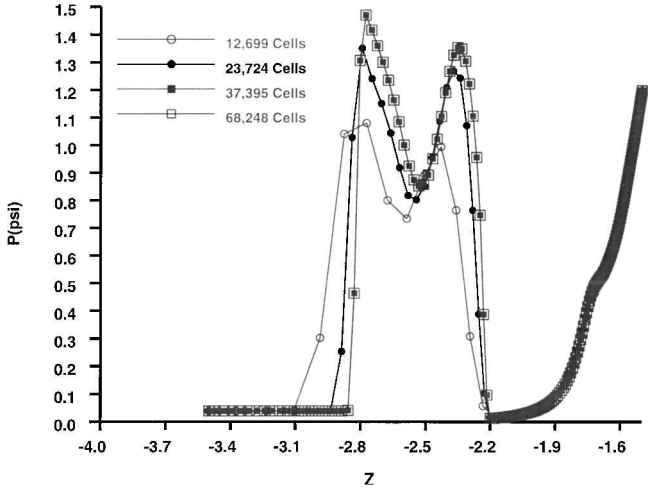

Fig. 2 Grid resolution for shock resolution.

For the finest mesh system, the average law-of-the-wall variable y^+ is around unity. The finest grid distribution is adopted for the rest of the present computations.

IV. Accuracy Assessment

The uncertainty in experimental data arises mostly from measurements of drag using load cells and the thermodynamic properties of the plasma. These piezoelectric quartz sensors have built-in microelectronic amplifiers, which convert the high-impedance electrostatic charge from the crystals into a low-impedance voltage output. Therefore, it is most effective for measuring a dynamic event. In the present investigation, the testing sequence is designed to take advantage of this feature. Efforts have been made to maintain an isolated environment for the sensors from electromagnetic and thermal interferences. From the large sets of data, including continuous data sweeps and discrete measurements, the data scattering band is less than 1.7%. However, the major portion of the data discrepancy between sweeps is in the determination of the absolute drag value after the model is injected in the tunnel jet stream. The overall measurement uncertainty is around 7%.

Another source of the experimental uncertainty is the thermodynamic state and transport property of the plasma. A major cause of concern is that the oscillating flowfield is self-sustained, which is the consequence of the closed feedback loop of the Mach disk and the free shear layer over the recirculating zone.[13] A point measurement in space, such as the langmuir probe, will collect the fluctuating information with a large temporal data scattering band. Although the internal energy partition among different quanta of the vibrational mode is uncertain, the average vibrational temperature of the plasma is determined to be 4400 ± 400 K. The electron temperature obtained from the langmuir probe near the sonic region in the shock layer was around 20,000 K. The corresponding electron density, which is highly dependent on the location relative to the plasma plume, yielded a value of $3 \times 10^{12}/\text{cm}^3$ or higher. Therefore, it is unrealistic to assume the plasma torch is in a state of thermodynamic equilibrium.[14] In spite of that, the nonequilibrium chemical kinetic effects to flow can still be small in view of the extremely low concentration of ionized components in the plasma jet, which appear only as trace elements (10^{-5}–10^{-10}) (Refs. 5 and 6).

For a shock-dominant problem, the criterion of numerical error evaluation is the shock definition and its standoff distance. In essence, the captured shock region is only first-order accurate for all approximate Riemann formulations. The computational error is assessed by generating solutions on consecutively refined grids immediately adjacent to the shock. The grid refinement was focused on the anticipated bow shock location. The calculated shock standoff distances, defined by the sonic point of the captured shock, were essentially grid independent after the third grid refinement. The identical process was also applied to nozzle configurations of smaller throat diameters.

V. Counterflow Jet/Shock Interaction

The spike tip or the jet spike on a blunt body has been used for wave drag reduction in aerodynamic applications.[15,16,24–26] Both flowfields have two distinct dynamic states, steady or oscillatory. For spike-tipped blunt bodies at a given Mach number, the ratio of spike length to the blunt-body diameter dictates whether an oscillatory motion can exist.[26] Similar behavior has also been observed for the jet spike or the counterflow jet flow when the injection pressure is varying in regards to a critical value.[13] These oscillatory flowfields have a common feature in a feedback loop structure of self-sustained oscillation associated with the free shear layer and shock wave.

In Fig. 3, the computed instantaneous streamline of a counterflow jet that issues from the stagnation point of a blunt body is presented. The numerical result is obtained for the jet stagnation pressure and temperature of 965.3 kPa (140 psi) and 294.4 K (530°R), respectively. The nozzle has a throat diameter of 0.76 mm. The exit Mach number of 3.28 leading into the hypersonic stream is generated by a wind-tunnel stagnation pressure of 344.9 kPa. Under this circumstance, the injection stagnation pressure is below the critical value for the counterflow jet/shock interaction; the flowfield is oscillatory. Nevertheless, it is easy to observe that the flowfield consists

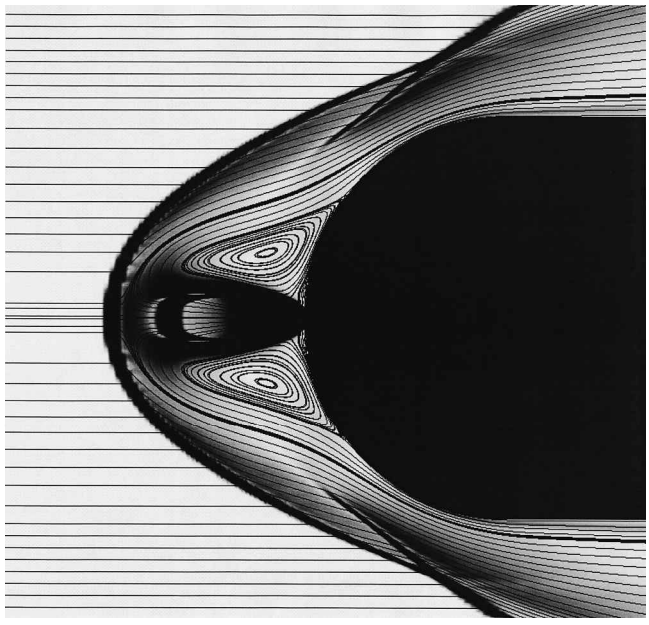

Fig. 3 Instantaneous streamlines of a counterflow jet.

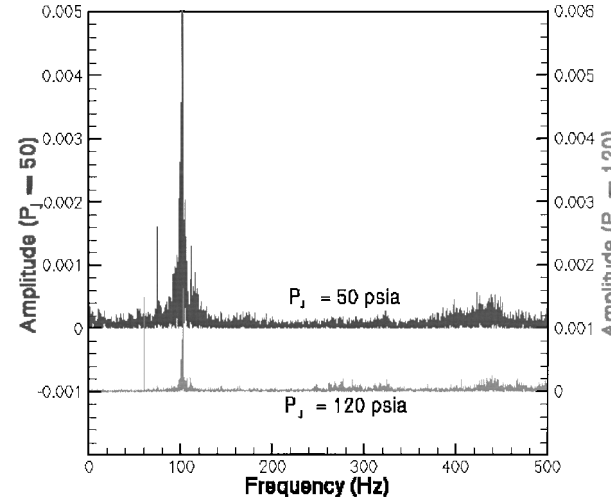

Fig. 4 Spectral data of drag measurements.

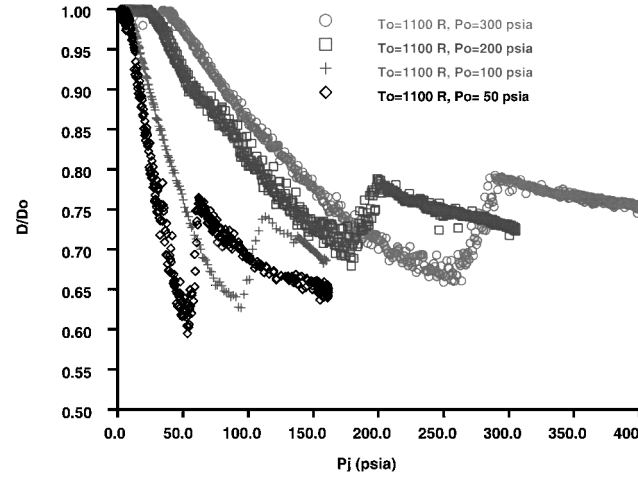

Fig. 5 Effect of exit pressure to counterflow jet drag data.

of the rapidly expanding counterflow jet issuing from the stagnation region and reversing its direction downstream by the Mach disk as a free shear layer. A part of the shear layer is entrained to form a toroidal recirculation zone beneath the dividing stream surface. A secondary separated flow structure can also be detected at the jet exit. Meanwhile, the rest of the free shear layer streams over the recirculation zone downstream. For the simulation condition, the flowfield bounded by the Mach disk and the recirculation zone is subsonic. Therefore, the pressure pulses can propagate freely from the recirculation zone upstream to the Mach disk to form a closed feedback loop. Finally, as the free shear layer reattaches to the blunt body, it induces a series of compression waves coalescing into a reattachment ring shock. The counterflow jet interaction replaces the single bow shock over a blunt body by a triple-shock structure. In spite of the additional reverse thrust by the counterflow jet, the reduced wave drag from the multiple shocks is still overwhelming. This shock structure modification by the inviscid–viscous aerodynamic interaction is the principal mechanism for wave drag reduction.

The shock bifurcation of the counterflow jet has been discovered recently.[5,13] At the bifurcation point between steady and unsteady states, the drag also attains its minimum value. In essence, the bifurcation is the consequence of breakdown of the subsonic feedback loop between the Mach disk and the unstable free shear layer. As the jet injection rate increases, the subsonic region connecting the Mach disk and the free shear layer diminishes in size. At the bifurcation point, a portion of the counterflow, the supersonic jet, diverts from the Mach disk, effectively cutting off the upstream signal propagation from the free shear layer. Then oscillatory motion ceases.[13]

The substantiation of the counterflow jet/shock bifurcation is easily observed from spectral data of the oscillatory drag force sensor given in Fig. 4. The data are collected for the nozzle with a throat diameter of 2.4 mm, and the tunnel is operated at a stagnation pressure of 689.47 kPa. Only two typical data over the entire bifurcation range are included, one of the them describes the subcritical state ($P_j = 50$ psia) where the oscillatory motion is sustained. In the subcritical state, at least two dominant discrete frequencies of 100 and 440 Hz are clearly revealed. Beyond the bifurcation point, the flowfield is nearly steady, or is as steady, as the condition for which the counterjet is shut off. The spectrum data for a supercritical state ($P_j = 150$ psia) are superimposed in Fig. 4. For the data recording range up to 500 Hz, the standard deviation of drag measurement between critical states is reflected by a factor of 11.72 decrease from the subcritical to supercritical state.

In Fig. 5, the counterflow jet/shock bifurcations and the drag reductions for a single conical nozzle at different wind-tunnel stagnation conditions are given. The counterflow nozzle has a throat diameter of 2.44 mm and a designed exit Mach number of 2.86. The stagnation temperature of the counterflow jet is maintained at a constant value of 294 K (530°R). At the four different tunnel stagnation pressures, the normalized total drag with respect to the value without injection (D/D_0) decreases continuously as the injecting stagnation pressure is increased. The drag reduction reaches its maximum at the bifurcation point. The overall maximum drag reduction is achieved at the lowest tunnel stagnation pressure of 342.4 kPa. Because the injection mass flow rate is a constant for the identical nozzle at a given stagnation condition of the jet, the difference between different tunnel stagnation pressures only reflects the final Mach number of the counterflow jet. Therefore, these sets of data revealed the dependence of drag reduction to the maximum counterflow Mach numbers.[13,16] The critical point of bifurcation is also clearly affected by this Mach number. In short, the higher exiting counterflow Mach number leads to a lower critical point injecting pressure for bifurcation and a greater amount of drag reduction. From all of the conditions tested, the drag reduction by the room-temperature air injection spans a range greater than 34.02–44.40% at the tunnel stagnation pressures of 2054 and 432.4 kPa (300 and 50 psia), respectively.

Numerical results duplicating the experimental conditions of the $d = 2.44$ mm nozzle are depicted in Fig. 6, at the tunnel stagnation pressures of 432.4 and 684.8 kPa (50 and 100 psia) and stagnation temperature of 1100 R. Both three-dimensional and axisymmetrical computations were carried out to determine whether the bifurcation is uniquely associated with three-dimensional dynamic motions. In short, both the three-dimensional and axisymmetrical computations reproduced the shock bifurcation.[13,14,24] Therefore, it is not

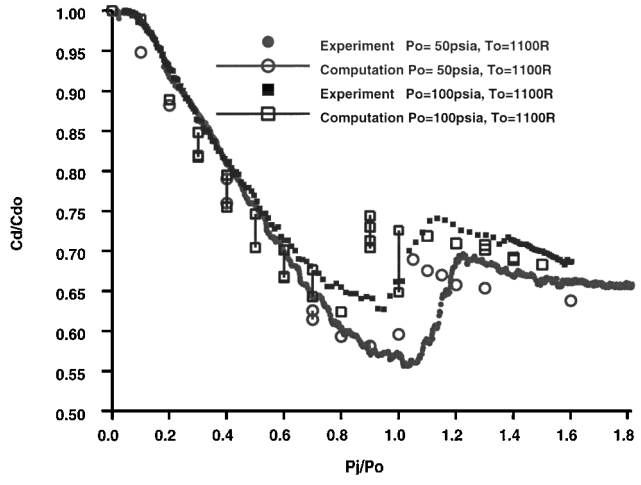

Fig. 6 Comparison of drag computations and data.

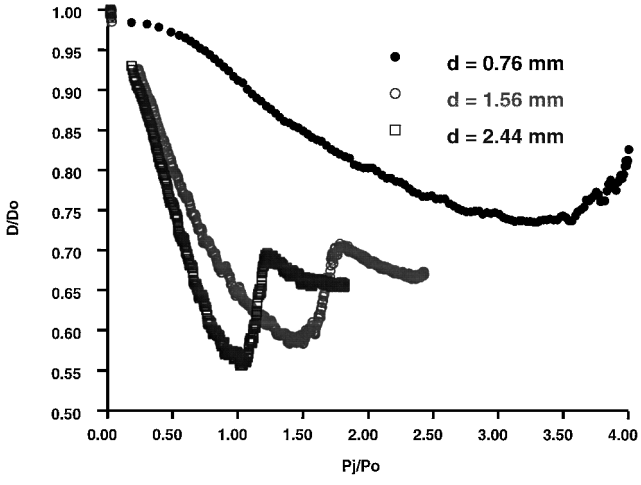

Fig. 7 Drag reduction from different conical nozzles.

necessary to have an additional transverse degree of freedom for a change of dynamic states in longitudinal orientation. Computations also correctly recover the oscillatory flow structure for all subcritical cases. All calculated drags for these cases revealed a scattering band in subcritical state that is absent or substantially reduced for the supercritical cases studied. Numerical results, however, consistently underpredict the drag over the entire range of injecting pressure. The drag computations for the tunnel stagnation pressure at 432.4 kPa yields a greater discrepancy of 6.1%, in contrast to 2.7% for the cases where the tunnel stagnation pressure is 684.8 kPa. Again, both calculations underpredict the critical value of P_j/P_o by approximately 11%. Because the present Navier–Stokes solutions did not include the based drag, this missing information was derived from the based pressure measurements.[5,13,14] The correction enters the calculated drag as a constant component and is one of the sources of discrepancy. Another source of error may be attributed to the turbulent closure.

Three different conical nozzles were used for the counterflow jet experiment. At a given constant tunnel and injecting stagnation pressure, the mass flow rate varies by a factor of 10.24 from the smallest to the largest nozzle throat diameter. The exiting Mach numbers vary in the design range from 2.86 to 3.28. Therefore, the major difference in drag reduction is the consequence of different injection mass flow rates and the chemical composition of the injectant. These drag reduction data are given in Fig. 7. From Fig. 7, it can be easily detected that the mass flow rate is a major contributing factor for the drag reduction via counterflow jet. The lower injecting mass flow rates not only lead to a lower value for the drag reduction, but also defer the critical point of the injecting pressure of bifurcation.

VI. Properties of Air Plasma

Initially, the rotational temperature of air plasma was attempted by the optical emission from the second positive electronic transition $C^3\Pi_u \rightleftharpoons B^3\Pi_g$ of molecular nitrogen.[27–29] However, the nitrogen C–B spectra were obscured by emission from other species, such as the molecular oxygen, nitric oxide, as well as vapors of copper and iron. Nevertheless, the origin band (0, 0) of the ionized nitrogen, N_2^+, $C^2\Pi_u^+ \rightleftharpoons X^2\Pi_g^+$ appears as a prominent feature in the plasma torch emission spectrum. A composite spectrum of the plasma torch in the 3400–4400 Å wavelength range was obtainable.[24] The average vibrational temperature, determined from the Boltzmann plot and a blackbody modeling is 4400 ± 400 K (7920 ± 720°R), which is comparable to that reported by Ganiev et al.[10] and Malmuth et al.[12]

At the plasma vibrational temperature around 4400 K and maximum static pressure within the shock layer of 10.5 kPa (78.9 torr), the plasma chemical composition in the equilibrium condition can be determined from numerous data.[30] Although the plasma counterflow jet is understood to be in a thermodynamically nonequilibrium state, the chemical composition and internal energy partition can not be predicted with certainty. However, it is reasonable to assume that the vibrational temperature is in thermal equilibrium with the translational and rotational degrees of freedom, but not necessarily with electron temperature.[3,5] The mass fractions of molecular nitrogen and nitric oxide are 0.68 (N_2) and 0.05 (NO), respectively. The oxygen molecules are nearly all dissociated to yield a mass fraction of atomic oxygen around 0.26 (O). The components of NO^+, O^+, N_2^+, and N^+ are on the order of magnitude from 10^{-5} to 10^{-10}. These low mass fractions are essentially trace elements.

The electron density and temperature of the plasma field around the torch and the magnetoaerodynamic experiment of the blunt body are measured by a double langmuir probe.[31,32] The probe is constructed from 0.5-mm platinum wire. The electrical potential is provided by a ±100-V Kepco bipolar power supply. To determine the entire current–voltage characteristic, electrical current measurement in the microampere range is essential. For that purpose, the resistor in the circuit can vary from 1030 to 11,305 Ω (Ref. 32). The langmuir probe has a double hole ceramic sleeve, a wire separation distance of 1.0 mm, and the sensing area of each probe is 2.1 mm^2. Although the platinum wire has a high resistance to oxidation at high temperature, the langmuir probe is still limited to the fringe area away from the plasma plume.

For the plasma injection, a langmuir probe survey of the entire shock layer was carried out at the lowest plasma injection pressure (70 psi). In general, the electron number density, electrical conductivity, electron temperature, and electrical field strength attain the maximum value in the plasma plume. This observation can be made easily by examining the electron number density and electron temperature distributions along the axial distance of the cylindrical polar coordinates r, θ, and z. Figure 8 displays the electron number density from the body surface to the bow shock along the axial coordinate z at the fixed radial distance $r = 0.76$ cm. This radial

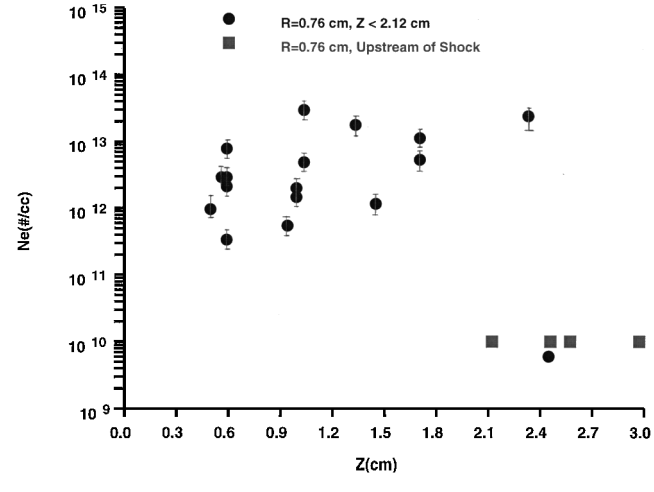

Fig. 8 Electron number density distribution; $r = 0.76$ cm.

location is also the minimum separation distance between the probe and the center of the plasma torch, so that the ceramic sleeve will not be thermally shattered by the plume.

Based on numerical results, the local temperature is around 3600 K (2000°R) (Refs. 13 and 14). The data were sampled from a distance as close as 0.1 cm from the nose capsule to a point beyond the detached bow shock. Because the flowfield is in the subcritical state of shock bifurcation, the measurements exhibit a very wide temporal scattering band. The data scattering also decays rapidly from the plasma plume and then slowly dissipates downstream. In spite of the large data scattering due the unsteady fluid motion, the averaged electron number density has a value around $5 \times 10^{12}/\text{cm}^3$, which is the highest value recorded. The bow shock location along the constant radial distance can be detected by a sharp drop of the electron number density. The bow shock also exhibits an oscillatory range from 2.12 to 2.46 cm from the blunt body. The electron number density upstream of the shock is less than 10^{10}, which is beyond the validated measurement range of the present double langmuir probe.

The electron temperature distributions at the identical locations are presented in Fig. 9. Again the data scattering band is the greatest among all measurements by the langmuir probe. Although along the constant radial array the calculated translational temperature is changing rapidly, the electron temperature along this array is nearly constant to yield an average value slightly higher than 20,000 K. This observation indicates a weak coupling between high-energy charged particles and the thermal and vibrational modes of the neutral. At the shock, the electron temperature dips drastically across the wave front. This behavior seems to indicate that the heavy charged particles of plasma are unable to propagate through the extremely high gradient region. Again, the data also revealed a bow shock oscillation from 2.12 to 2.46 cm from the blunt body.

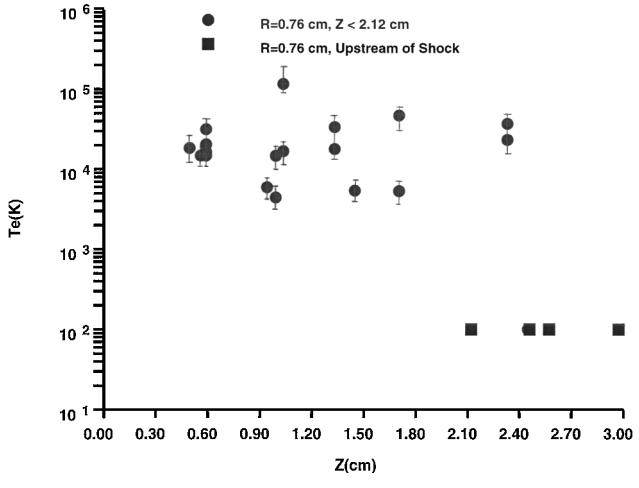

Fig. 9 Electron temperature distribution; $r = 0.76$ cm.

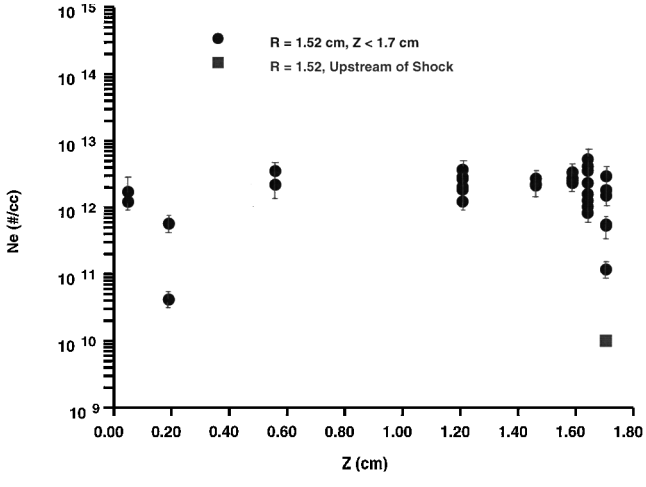

Fig. 10 Electron number density distribution; $r = 1.52$ cm.

Typical electron number density, electrical conductivity, and electron temperature distributions are presented in Figs. 10–13. These data are collected along the axial coordinate z at a constant radial distance $r = 1.53$ cm from the axis of the model. The distributions are collected from the blunt body to a location beyond the enveloping bow shock. In Fig. 10, the electron number density distribution across the shock layer is depicted. The measured number density of electrons fluctuates around the value of $2 \times 10^{12}/\text{cm}^3$. The number density increases slightly approaching the bow shock and then drops drastically across the shock. In this regard, the shock wave is acting like a barrier in preventing heavy charged particles from escaping

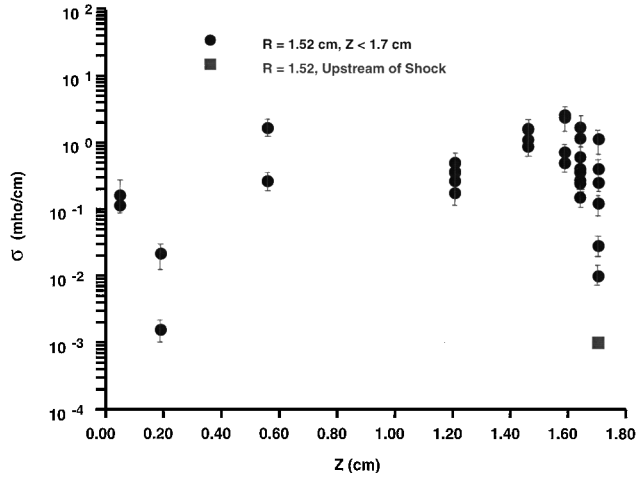

Fig. 11 Electrical conductivity distribution; $r = 1.52$ cm.

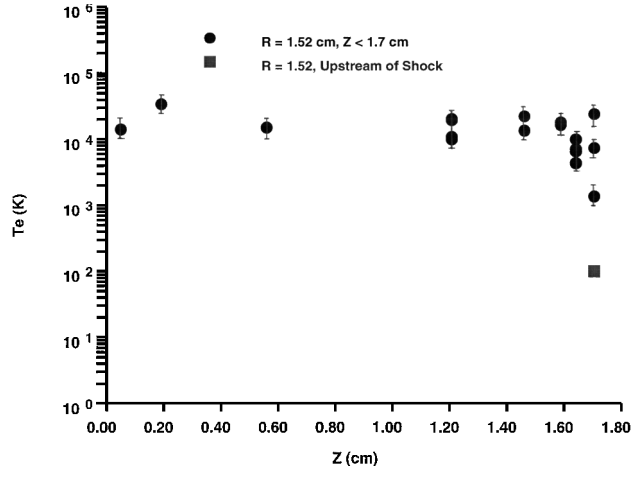

Fig. 12 Electron temperature distribution; $r = 1.52$ cm.

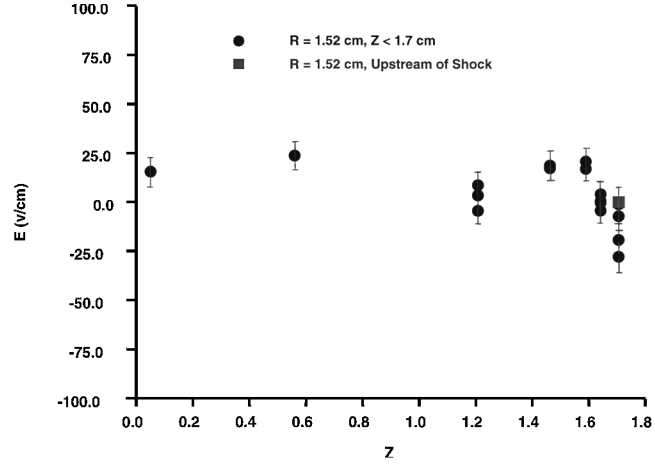

Fig. 13 Electrical potential distribution; $r = 1.52$ cm.

the shock envelope. One would expect that charge separation would take place across the shock front like that in the region of electrodes. However, the present measurement does not have sufficient resolution to allow a definitive conclusion to be drawn. The electrical conductivity distribution along the same trace exhibits the nearly identical behavior as that of the electron number density in Fig. 11. This behavior is anticipated because the electrical conductivity σ is linearly proportional to the electron number density and electron mobility.[31] For the present experiment, the electrical conductivity yields an average value of 60 mho/m across the major portion of the shock layer, rises to a slightly higher value of 140 mho/m at the shock, and falls to a very low and unmeasurable value upstream of the shock.

The electron temperature distribution of plasma in the shock layer is presented in Fig. 12. The statistical average value across the shock layer in the constant radial array is 20,000 K (36,000°R). Beyond the bow shock envelope, the electron temperature of the plasma falls below the value that can be measured with any certainty. In spite of the extremely low concentration of ions such as NO^+, O_2^+, N_2^+, and N^+, this measurement clearly shows that the plasma field is not in the state of thermal equilibrium. Finally, the electrical potential of the plasma torch along the same constant radial distance from the axis is depicted in Fig. 13, and the overall measured potential is confined within the band of ±30 V/cm. At the shock front, the electrical potential reveals predominant negative values in contrast to the rest of the field in the shock layer. It may be viewed as additional evidence of charge separation.

VII. Plasma Injection Experiment

In the plasma injection experiment, the plasma is generated by a plasma cutting torch embedded in the force measuring model. Because the power output of the torch in the startup mode is rather limited, only a small amount of air supply can be ionized. In the experiment, the stagnation pressure of the air supply spans a narrow range from 482.6 to 965.3 kPa (70 to 140 psi). In this injection pressure range, the flow is in the subcritical bifurcation state and is characterized by oscillatory motion.

In the present data collection process, the drag measuring procedure starts with room-temperature air injection. The plasma is then introduced by igniting the torch and is sustained for a duration of 15 s. The piezoelectric force sensors have yielded consistent output immediately after the transient electromagnetic pulse has subsided. The individual drag measurement of the room-temperature air injection registers a value close to the values from the data sweep. The measured drags rise when the plasma is ignited. According to the present and earlier computational analyses of a comparable simulation, this behavior is mostly due to reduced mass injection flow rate.[14,29] There is little doubt that the plasma injection has produced a greater drag reduction than the room-temperature air injection at the identical mass flow rate. However, the additional drag reduction is derived from thermal energy deposition.

The composite schlieren photograph at four different stagnation pressures of the plasma injection is presented in Fig. 14. The plasma is injected into the bow shock envelope at stagnation pressures of 582, 689, 827, and 965 kPa (70, 100, 120, and 140 psi). In these presentations, the schlieren photographs in Figs. 14a and 14b represent the lower and higher injecting stagnation pressures, respectively. In the composite photographs, the upper images are results of room temperature injection and the corresponding lower images record the results of plasma injection. Two major features of the plasma injection in contrast to the room-temperature counterflow jet stand out. First, the shock waves uniformly retract toward the blunt body for all cases tested. Based on the perfect gas model calculation, this phenomenon is mostly associated with a reduced mass flow rate by the elevated plasma temperature.[13,14] The mass flow rate of the nozzle is linearly proportional to the stagnation pressure and inversely proportional to the square root of the stagnation temperature $\dot{m} \sim (p_o/\sqrt{T_o})_j$. Under the present testing condition, the mass flow rate is reduced by a factor of 3.9.

The other feature of plasma injection is that the amplitude of the unsteady shock wave movement is significantly subdued. However, the basic oscillatory behavior of flowfields between two different

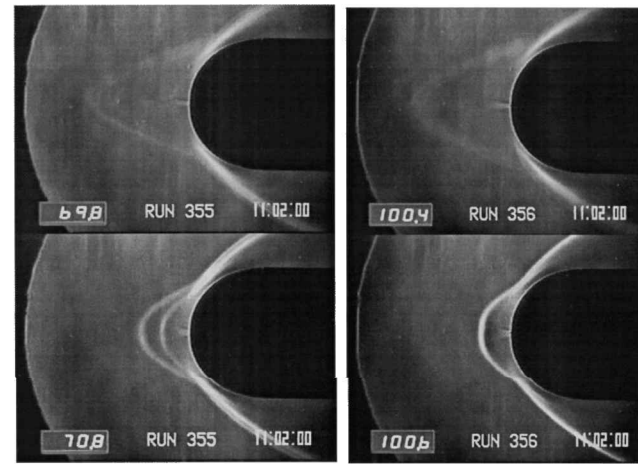

a) P_j = 582 and 689 kPa (70 and 100 psi)

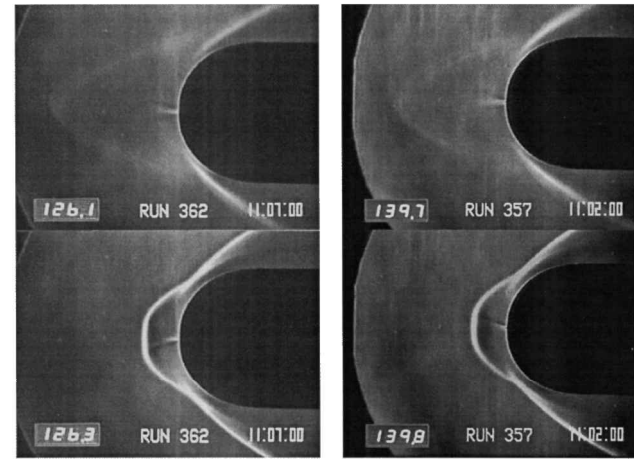

b) P_j = 827 and 965 kPa (120 and 140 psi)

Fig. 14 Schlieren photographs of plasma injection.

injectants is similar, and the most predominant oscillatory mode occurs at 100 Hz. Over the frequency range from 500 to 2500 Hz, the oscillatory amplitude of the plasma injection is roughly 10 dB lower than the room-temperature air counterpart.[14,24] This behavior is dramatic on the video recording, and the same observation can also be made from the blurred photographic images of the room-temperature injection to the sharply defined shock structure by the plasma injection. At the lowest plasma injection pressure (482 kPa or 70 psi), two biased bow shocks appear to dominate over others, but the unsteady movement of shock waves persists. These two contrasting features between the room-temperature air and plasma injection are uniformly observed over the entire tested pressure range.

To differentiate the electromagnetic phenomenon from the aerodynamic interaction and thermal effect, an applied magnetic field is imposed on the plasma stream. A set of neodymium rare earth (NeFeB) magnet collars have been placed around the counterflow nozzle, and the maximum magnetic flux density at the pole registers a value of 0.47 T. The magnetic field is aligned with the axis of the nozzle. The polarity of the magnet is also reversed to seek a possible change in drag. Thus, the applied magnetic field is expected to produce a difference in total drag.

VIII. Results of Plasma Injection

The controlling parameters of the counterflow jet are the jet mass flow rate, jet exit Mach number, and thermodynamic property of the injectant.[11–14] In the present effort, the jet exit Mach number of the nozzle is 3.26 for the calorically perfect air. For plasma injection, the nonequilibrium weakly ionized air changes the chemical composition and thermodynamic property of the injectant. At present, an accurate description of the nonequilibrium plasma is far from ascertained, but a reasonable measurement of injectant temperature

is possible by emission spectra. Therefore, the detection of any possible nonequilibrium phenomenon is approached by demonstrating its departure from perfect gas behavior and as an air mixture with a known equilibrium air composition. Because a fixed air plasma composition is assumed downstream of the nozzle throat, the plasma injection field is effectively treated as a chemically frozen flow.

The equilibrium chemical composition of the plasma counterflow jet is obtained in terms of mass fraction at the thermodynamic state near the Mach disk in the shock layer (4400 K and 10.5 kPa). From these conditions, the specific heat of the air plasma has a value of $\gamma = 1.28$. The mass flow rates of the plasma counterflow jet were calculated by solving the Reynolds-averaged Navier–Stokes equations based on this composition. The computed mass flow rates have values of 0.13, 0.19, 0.23, and 0.26 g/s, which corresponds to the nominal injection pressure ratios, P_j/P_o of 1.4, 2.0, 2.5, and 2.8, respectively.

The side-by-side comparison of schlieren photographs and computed results of the counterflow plasma injection is given in Fig. 15. For comparison, the stagnation pressure of the jet is 482.6 kPa (70 psi), the ratio of the stagnation pressures of the jet and the tunnel is 1.4. The injecting rates are 0.52 and 0.13 g/s at the stagnation temperatures of 294 and 4400 K, respectively. The plasma jet computation is based on the assumptions that the sonic condition prevails at the nozzle throat, and the chemical composition of the plasma is not drastically different from the equilibrium condition. Therefore, the thermodynamic properties of the plasma can be approximated by the equilibrium air composition at the temperature of 4400 K and pressure of 10.5 kPa (Ref. 30). In short, the entire plasma injection flowfield is modeled by the chemically frozen flow approximation. This numerical result is significantly different from the computations using the ideal gas model in Fig. 15a and reaches a reasonable affinity with experiment. Specifically, the complex shock system retracts to the body to reflect the reduced mass flow rate at the elevated injecting stagnation temperature.

In Fig. 16, the drag data are presented as a function of the mass flow rate. In this physically meaningful format, the drag reduction by plasma injection can be easily explained. The calculation at the identical mass flow rate reveals that the plasma injection indeed

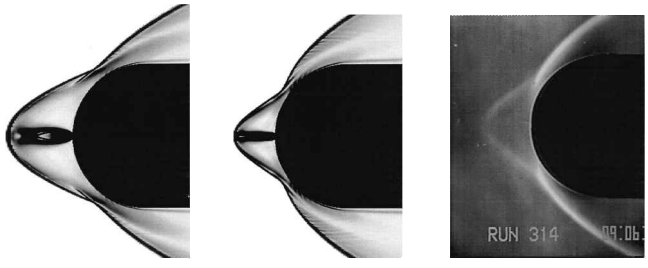

a) b) c)

Fig. 15 Comparison of schlieren and computation.

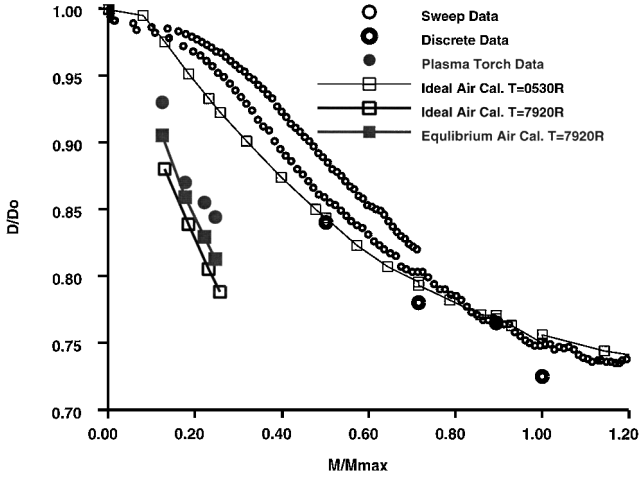

Fig. 16 Drag data vs injecting mass flow rate.

produces a greater drag reduction than its room-temperature counterpart. The reduced drag is derived from the thermal deposition of the plasma. However, when energy is distributed among different internal degrees of excitation, the amount of drag reduction diminishes. Most important, the difference between calculated results and measurements is confined within the band of data uncertainty. This observation is further substantiated by the reasonable replication of shock structures by computations, suggesting that the effect of nonequilibrium chemical kinetics may not be significant under the present tested condition.

From all efforts in magnetoaerodynamic research,[7–9] the plasma flowfield modifications are a consequence of the applied electromagnetic field. However, in the most recent experiments using plasma injection for drag reduction, the applied electromagnetic field is conspicuously absent.[10–12] Theoretically, the drag reduction by an induced electromagnetic field, if possible at all, will be negligible. In an attempt to further define the electromagnetic effect for the plasma counterflow jet, an applied magnetic field was imposed by a set of neodymium rare earth (NeFeB) magnets around the plasma torch chamber. The applied magnetic field is aligned with the axis of the nozzle to enhance the plasma pinch effect.[31] The magnet has a maximum magnetic flux density of 0.47 T at the pole, but the field strength diminishes rapidly toward the nozzle axis. The estimated value is about 0.17 T locally, and the plasma interaction parameter, $S = (\sigma B^2 R/\rho u)$, is far less than unity. Under this circumstance, the effect of electromagnetism is minuscule where detection is concerned. As anticipated, only limited success was achieved at the lowest plasma stagnation pressure. The plasma torch with the applied magnetic field ceased to function when the air supply to the torch chamber was higher than 482.6 kPa. The difference of the measured data with the applied magnetic field is recorded, but its magnitude is confined within the uncertain data scattering band. Therefore, the weak applied magnetic field did not produce a definitive effect on drag reduction. The effect of a still weaker inducted electromagnetic field will be even smaller, so as to become negligible.

The electromagnetic force of the plasma injection may enter the interaction through conductive current and the transport of excess charges.[27] Significant charge separation may occur at locations where the disparity of electron and ion mobility are accentuated, such as near the electrodes and across the shock wave. Because an electromagnetic field modifies the Rankine–Hugoniot condition across a shock,[2,3] the charge separation at the shock wave is one of the likely sources to affect the wave drag. The present measurements by the double langmuir probe did not generate concrete evidence to support this. For the present experiment, it is logical to conclude that the effect of electromagnetic force on drag reduction is insignificant.

IX. Conclusions

The drag reduction by a plasma counterflow jet is investigated in a Mach 6 wind tunnel at a freestream pressure of 268.7 Pa (0.040 psi) and temperature of 79 K (142.3°R). The plasma with a vibrational temperature of 4400 ± 400 K, an electron temperature about 20,000 K, and an electron density greater than $3 \times 10^{12}/\text{cm}^3$ is injected from a hemispherical cylinder. At a given injecting stagnation pressure, the measured drag is nearly 10% higher than the room-temperature air injection. However, if the decreased injection mass flow by the elevated plasma temperature is taken into consideration, the drag reduction by plasma injection is, in fact, greater than its room-temperature counterpart.

Based on the equilibrium chemical composition at the plasma condition and at the identical injecting mass flow rate, the plasma injection would yield a 12.5% greater drag reduction by the plasma thermal effect alone. The present side-by-side experimental and computational research indicates that the major portions of drag reduction by plasma injection are derived from the favorable shock and counterflow jet interaction and thermal energy deposition. The contribution from the electromagnetism is barely detectable and is deemed insignificant in the present experiment.

From the present investigation, the electromagnetic effect shows promise to be the sought-after mechanism for aerodynamic enhancement. The magnetoaerodynamic phenomenon in hypersonic flow must be derived from a significant and appropriate applied

electromagnetic field. This is merely a reaffirmation of pioneering theoretical observations.

Acknowledgments

The author deeply appreciates the sponsorship by Steven Walker of the Air Force Office of Scientific Research. The computing resource was supported by a grant from the Department of Defense High Performance Computing Shared Resource Center at Wright–Patterson Air Force Base. The invaluable contributions by James Hayes, Ken Wurtzler, James Miller, James M. Williamson, Dean Emmer, J. Menart, and the wind-tunnel crew, Tom Norris, Ray Raber, and Michael Greene, are duly acknowledged.

References

[1]Resler, E. L., and Sears, W. R., "The Prospects for Magneto-aerodynamics," *Journal of the Aeronautical Sciences*, Vol. 25, 1958, pp. 235–245 and 258.

[2]Sutton, G. W., and Sherman, A., *Engineering Magnetohydrodynamics*, McGraw–Hill, New York, 1965, pp. 295–308.

[3]Mitchner, M., and Kruger, C. H., *Partially Ionized Gases*, Wiley, New York, 1973, pp. 163–241.

[4]Shang, J. S., "An Outlook of CEM Multidisciplinary Applications," AIAA Paper 99-0336, Jan. 1999.

[5]Shang, J. S., Ganguly, B., Umstattd, R., Hayes, J., Arman, M., and Bletzinger, P., "Developing a Facility for Magnetoaerodynamic Experiments," *Journal of Aircraft*, Vol. 17, No. 6, 2000, pp. 1065–1072.

[6]Shang, J. S., "Recent Research in Magnetoaerodynamics," *Progress in Aerospace Science*, Vol. 37, Jan. 2001, pp. 1–20.

[7]Ziemer, R. W., "Experimental Investigation in Magnetoaerodynamics," *American Rocket Society Journal*, Vol. 19, Sept. 1959, pp. 642–646.

[8]Bush, W. B., "Magnetohydrodynamics-Hypersonic Flow past a Blunt Body," *Journal of the Aeronautical Sciences*, Vol. 25, Nov. 1958, pp. 685–690 and 728.

[9]Meyer, R. C., "On Reducing Aerodynamic Heat-Transfer Rates by Magnetohydrodynamic Techniques," *Journal of the Aero/Space Sciences*, Vol. 25, No. 9, 1958, pp. 561–566, 572.

[10]Ganiev, Y. C., Gordeev, V. P., Krasilnikov, A. V., Lagutin, V. I., Otmennikov, V. N., and Panasenko, A. V., "Aerodynamic Drag Reduction by Plasma and Hot-Gas Injection," *Journal of Thermophysics and Heat Transfer*, Vol. 14, No. 1, 2000, pp. 10–17.

[11]Klimov, A., Leonov, S., Pashina, A., Skvottsov, V., Cain, T., and Timofeev, B., "Influence of a Corona Discharge on the Supersonic Drag of a Axisymmetric Body," AIAA Paper 99-4856, 1999.

[12]Malmuth, N. D., Fomin, V. M., Maslov, A. A., Fomichev, V. P., Shashkin, A. P., Korotaeva, T. A., Shipyuk, A. N., and Pozdnyakov, G. A., "Influence of a Counterflow Plasma Jet on Supersonic Blunt-Body Pressure," AIAA Paper 99-4883, Nov. 1999.

[13]Shang, J. S., Hayes, J., Wurtzler, K., and Strang, W., "Jet-Spike Bifurcation in High-Speed Flows," *AIAA Journal*, Vol. 36, No. 6, 2001, pp. 1159–1165.

[14]Shang, J. S., Hayes, J., and Menart, J., "Hypersonic Flow over a Blunt Body with Plasma Injection," AIAA Paper 2001-0344, Jan. 2000.

[15]Finley, P. J., "The Flow of a Jet from a Body Opposing a Supersonic Free Stream," *Journal of Fluid Mechanics*, Vol. 26, Pt. 2, 1966, pp. 337–368.

[16]Barber, E. A., Jr., "An Experimental Investigation of Stagnation-Point Injection," *Journal of Spacecraft and Rockets*, Vol. 2, No. 5, 1965, pp. 770–774.

[17]Shang, J. S., "Numerical Simulation of Hypersonic Flows," *Computational Method in Hypersonic Aerodynamics*, Computational Mechanics Publ., Southampton, England, U.K., 1992, pp. 81–114.

[18]Josyula, E., "Computational Study of Vibrationally Relaxing Gas Past Blunt Body in Hypersonic Flow," *Journal of Thermophysics and Heat Transfer*, Vol. 14, No. 1, 2000, pp. 18–26.

[19]Strang, W. Z., Tomaro, R. F., and Grismer, M., "The Defining Methods of $Cobalt_{60}$: A Parallel, Implicit, Unstructured Euler/Navier–Stokes Flow Solver," AIAA Paper 99-0786, Jan. 1999.

[20]Tomaro, R. F., Strang, W. Z., and Sankar, L. N., "An Implicit Algorithm for Solving Time-Dependent Flows on Unstructured Grids," AIAA Paper 97-0333, Jan. 1997.

[21]Grismer, M. J., Strang, W. Z., Tomaro, R. F., and Witzman, F. C., "Cobalt: A Parallel, Implicit, Unstructured Euler/Navier–Stokes Solver," *Advances in Engineering Software*, Vol. 29, April–July, 1998, pp. 365–373.

[22]Spalart, P. R., and Allmaras, S. R., "One-Equation Turbulence Model for Aerodynamic Flows," AIAA Paper 92-0439, Jan. 1992.

[23]Ambrosio, A., and Wortman, A., "Stagnation Point Shock Detachment Distance for Flow Around Spheres and Cylinder," *American Rocket Society Journal*, Vol. 32, No. 2, 1962, p. 281.

[24]Shang, J. S., Hayes, J., Miller, J., and Menart, J., "Blunt Body in Hypersonic Electromagnetic Flowfield," AIAA Paper 2001-2803, June 2001.

[25]Bogonoff, S. M., and Vas, I. E., "Preliminary Investigations of Spiked Bodies at Hypersonic Speeds," *Journal of the Aerospace Sciences*, Vol. 26, No. 1, 1959, pp. 65–74.

[26]Shang, J. S., Hankey, W. L., and Smith, R. E., "Flow Oscillations of Spike-Tipped Bodies," *AIAA Journal*, Vol. 20, No. 1, 1982, pp. 25, 26.

[27]Gilmore, F. R., Laher, R. R., and Espy, P. J., "Franck–Condon Factors, r-Centroids, Electronic Transition, Moments, and Einstein Coefficients for Many Nitrogen and Oxygen Band Systems," *Journal of Physical and Chemical Reference Data*, Vol. 21, No. 5, 1992, pp. 1005–1107.

[28]Herzberg, G., *Molecular Spectra and Molecular Structure. I. Spectra of Diatomic Molecules*, 2nd ed., Van Nostrand, New York, 1950.

[29]Huber, K. P., and Herzberg, G., *Molecular Spectra and Molecular Structure, Vol IV: Constants of Diatomic Molecules*, Van Nostrand Reinhold, New York, 1979.

[30]McBride, B. J., and Gordon, S., *Computer Program for Calculation of Complex Chemical Equilibrium Compositions and Applications, II. User Manual and Program Description*, NASA Reference Publ. 1331, June 1996, pp. 44–46.

[31]Howatson, A. M., *Introduction to Gas Discharges*, 2nd ed., Pergamon, Oxford, 1975, pp. 168–190.

[32]Menart, J., Shang, J. S., and Hayes, J., "Development of a Langmuir Probe for Diagnostic Technique for Plasma Diagnostic Work in High-Speed Flow," AIAA Paper 2001-2804, June 2001.

P. Givi
Associate Editor